

April 27, 2018

Upper Limits on the Presence of Central Massive Black Holes in Two Ultra-compact Dwarf Galaxies in Centaurus A

Karina T. Voggel, *University of Utah*

Anil C. Seth, *University of Utah*

Nadine Neumayer, *Max Planck Institute for Astronomy*

Steffen Mieske, *European Southern Observatory*

Igor Chilingarian, *Smithsonian Astrophysical Observatory*, et al.



Upper Limits on the Presence of Central Massive Black Holes in Two Ultra-compact Dwarf Galaxies in Centaurus A

Karina T. Voggel¹, Anil C. Seth¹, Nadine Neumayer², Steffen Mieske³, Igor Chilingarian^{4,5}, Christopher Ahn¹, Holger Baumgardt⁶, Michael Hilker⁷, Dieu D. Nguyen¹, Aaron J. Romanowsky^{8,9}, Jonelle L. Walsh¹⁰, Mark den Brok¹¹, and Jay Strader¹²

¹ University of Utah, Department of Physics & Astronomy, 115 S 1400 E, Salt Lake City, UT 84105, USA; kvoggel@astro.utah.edu

² Max-Planck Institut für Astronomie, Königstuhl 17, D-69117 Heidelberg, Germany

³ European Southern Observatory, Alonso de Cordova 3107, Vitacura, Santiago, Chile

⁴ Smithsonian Astrophysical Observatory, 60 Garden Street MS09, 02138 Cambridge, MA, USA

⁵ Sternberg Astronomical Institute, M.V. Lomonosov Moscow State University, 13 Universitetsky prospect, 119992 Moscow, Russia

⁶ School of Mathematics and Physics, University of Queensland, St. Lucia, QLD 4072, Australia

⁷ European Southern Observatory, Karl-Schwarzschild-Straße 2, D-85748 Garching bei München, Germany

⁸ Department of Physics and Astronomy, San Jose State University, San Jose, CA 95192, USA

⁹ University of California Observatories, 1156 High Street, Santa Cruz, CA 95064, USA

¹⁰ George P. and Cynthia Woods Mitchell Institute for Fundamental Physics and Astronomy, Department of Physics and Astronomy, Texas A&M University, College Station, TX 77843, USA

¹¹ Institute for Astronomy, Department of Physics, ETH Zurich, CH-8093 Zürich, Switzerland

¹² Center for Data Intensive and Time Domain Astronomy, Department of Physics and Astronomy, Michigan State University, 567 Wilson Road, East Lansing, MI 48824, USA

Received 2018 February 1; revised 2018 March 14; accepted 2018 March 23; published 2018 April 27

Abstract

The recent discovery of massive black holes (BHs) in the centers of high-mass ultra-compact dwarf galaxies (UCDs) suggests that at least some are the stripped nuclear star clusters of dwarf galaxies. We present the first study that investigates whether such massive BHs, and therefore stripped nuclei, also exist in low-mass ($M < 10^7 M_\odot$) UCDs. We constrain the BH masses of two UCDs located in Centaurus A (UCD 320 and UCD 330) using Jeans modeling of the resolved stellar kinematics from adaptive optics data obtained with the SINFONI integral field spectrograph at the Very Large Telescope (VLT/SINFONI). No massive BHs are found in either UCD. We find a 3σ upper limit on the central BH mass in UCD 330 of $M_* < 1.0 \times 10^5 M_\odot$, which corresponds to 1.7% of the total mass. This excludes a high-mass fraction BH and would only allow low-mass BHs similar to those claimed to be detected in Local Group globular clusters. For UCD 320, poorer data quality results in a less constraining 3σ upper limit of $M_* < 1 \times 10^6 M_\odot$, which is equal to 37.7% of the total mass. The dynamical mass-to-light ratios of UCD 320 and UCD 330 are not inflated compared to predictions from stellar population models. The non-detection of BHs in these low-mass UCDs is consistent with the idea that elevated dynamical mass-to-light ratios do indicate the presence of a substantial BH. Although no massive BHs are detected, these systems could still be stripped nuclei. The strong rotation (v/σ of 0.3–0.4) in both UCDs and the two-component light profile in UCD 330 support the idea that these UCDs may be stripped nuclei of low-mass galaxies whose BH occupation fraction is not yet known.

Key words: galaxies: dwarf – galaxies: kinematics and dynamics – galaxies: nuclei – galaxies: star clusters: general

1. Introduction

Ultra-compact dwarf systems (UCDs) are among the densest stellar objects in the universe, and with their almost spherical appearances, they resemble globular clusters (GCs; Minniti et al. 1998; Hilker et al. 1999; Drinkwater et al. 2000). A common definition of UCDs is that they have to be more massive than ω Cen ($M > 2 \times 10^6 M_\odot$), but there is no clear physical property that separates UCDs from GCs. When compared to dwarf galaxies, however, they are much smaller and have higher stellar densities at the same luminosity (Misgeld & Hilker 2011; Norris et al. 2014). It is still under debate how these “intermediate” objects formed.

One proposed formation channel for UCDs is that they formed as genuine massive GCs (Mieske et al. 2004, 2012; Murray 2009) during intense starbursts or mergers that have high enough star formation rates to produce such massive clusters (Renaud et al. 2015; Schulz et al. 2015). Young clusters in the UCD mass range have been observed in nearby merger remnants, with virial masses of up to $8 \times 10^7 M_\odot$

(Maraston et al. 2004; Bastian et al. 2006). A second formation mechanism is that UCDs might be the stripped nuclear star cluster of a parent galaxy that was accreted onto a larger galaxy or galaxy cluster (Bekki et al. 2003; Drinkwater et al. 2003; Pfeffer & Baumgardt 2013).

There is evidence that supports the notion that both formation channels contribute to the population of UCDs we observe (Hilker 2006; Brodie et al. 2011; Da Rocha et al. 2011; Norris & Kannappan 2011). However, it is unclear so far what fraction of UCDs was formed as genuine GCs and how many of them are former galaxy nuclei. Related questions are whether the contribution of UCD formation channels changes with UCD mass and environment, and if it depends on the galaxy cluster they reside in.

The number of stripped nuclei in the Fornax and Virgo cluster environment was predicted using the Millennium II simulation and the associated semi-analytic model developed by Pfeffer et al. (2014, 2016). It is estimated that above masses of $10^7 M_\odot$, stripped nuclei make up 40% of all objects in the Fornax cluster and that the most massive globular cluster would

have a mass of $2 \times 10^7 M_\odot$. The fraction of stripped nuclei drops significantly to 2.5% between 10^6 and $10^7 M_\odot$. Overall, the combined mass function of simulated stripped nuclei and GCs agrees well with observations, indicating that UCDs are indeed a mix between GCs and stripped nuclei.

Quantifying the number of stripped nuclei in a galaxy cluster would provide a new way to infer its past merger history. Stripped nuclei UCDs could then provide a useful anchor point for simulations that predict the number of tidally disrupted dark matter halos in a galaxy cluster.

There are three main ways to identify UCDs as stripped nuclei: (1) detecting the remnant tails and extended low surface brightness envelopes caused by the tidal stripping process, (2) determining whether the star formation history of a UCD is extended, and (3) measuring whether they host a super-massive black hole (SMBH) in their centers, which are common in nuclei of galaxies.

Tidal tails and envelopes around UCDs are expected when a galaxy is in the process of being stripped, but these typically have short lifetimes. Such features were detected around UCDs in the Fornax and Perseus clusters (Voggel et al. 2016; Wittmann et al. 2016). A tidal stream of 1.5 kpc was recently found around a newly discovered very massive ($M = 4.2 \times 10^8 M_\odot$) UCD in NGC 7727 (Schweizer et al. 2018). In addition, a UCD of the size of ω Cen was discovered embedded in a stellar stream around NGC 3628 (Jennings et al. 2015).

An extended star formation history that extends over several Gyr has been found in NGC 4546-UCD1 (Norris et al. 2015). This long star formation timescale is similar to what is observed in galaxy nuclei (e.g., Rossa et al. 2006; Seth et al. 2006; Walcher et al. 2006). In contrast, GCs have usually very short (< 1 Gyr) star formation histories. In the Milky Way, two massive clusters have extended star formation histories. The first is M54, the nucleus of the partially stripped Sgr dwarf galaxy (Siegel et al. 2007; Carretta et al. 2010), and the other is Omega Cen (Hilker et al. 2004), which is widely thought to be a stripped nucleus.

If UCDs are stripped nuclei, then we expect super-massive black holes (SMBH) in their centers, similar to those observed in the nuclear star clusters of galaxies (Seth et al. 2008a; Graham & Spitler 2009). The high mass of an SMBH causes a distinctive central rise in velocity dispersion that is detectable in bright UCDs using adaptive optics combined with integral field spectroscopy. Such BH mass measurements have been carried out in four high-mass UCDs ($> 10^7 M_\odot$), and there is strong observational evidence from dynamical modeling that they all host SMBHs that make up $\sim 15\%$ of their total mass (Seth et al. 2014; Ahn et al. 2017; Afanasiev et al. 2018). The higher-than-expected velocity dispersions of these massive UCDs also provide indirect evidence for a high fraction of SMBHs and thus suggests a high fraction of former galaxy nuclei among high-mass UCDs.

At the low-mass end, there is evidence that both M54 and ω Cen have a massive BH in their centers and are thus stripped nuclei. In M54, a BH mass of $1 \times 10^4 M_\odot$ was suggested (Ibata et al. 2009), and a $4.0\text{--}4.7 \times 10^4 M_\odot$ black hole is suggested in the center of ω Cen (Noyola et al. 2010; Baumgardt 2017). The central dispersion increase of such intermediate-mass BHs (IMBH) could also be explained with significant radial anisotropy without an IMBH (van der Marel & Anderson 2010; Zocchi et al. 2017).

Table 1
Literature Values for UCD 330 and UCD 320

Name	UCD 330	UCD 320	Reference
R.A.	13:25:54.3	13:25:52.7	Taylor+2010
Decl.	−42:59:25.4	−43:05:46.6	Taylor+2010
M_V [mag]	−11.66	−10.39	Rejkuba+2007
$[M/H]$	-0.36 ± 0.14	-0.85 ± 0.14	Beasley+2008
r_{eff} [pc]	3.25 ± 0.13	6.83 ± 0.10	Taylor+2010
σ_v [km s $^{-1}$]	41.5 ± 3.7	20.0 ± 1.4	Taylor+2010
σ_v [km s $^{-1}$]	30.5 ± 0.2	19.0 ± 0.1	Rejkuba+2007
R_{gc} [kpc]	5.8	7.3	Rejkuba+2007

If UCDs are the remnant nuclear star clusters (NSCs) of a stripped galaxy, then their masses directly trace the mass of the progenitor host galaxy via the NSC–host galaxy mass relation (Ferrarese et al. 2006). However, this relation has a significant scatter, meaning that galaxies of the same mass can have nuclei masses that vary by two orders of magnitude (Georgiev et al. 2016). In the scenario where UCDs ($M > 2 \times 10^6 M_\odot$) are the stripped nuclei of former more massive galaxies, they will trace the merging of progenitor galaxies with stellar masses of $5 \times 10^8 M_\odot < M < 10^{11} M_\odot$, assuming the nuclei–galaxy mass correlation (Georgiev et al. 2016). The high metallicities of UCDs with confirmed SMBHs are consistent with them being nuclei that follow the mass–metallicity relation of their larger parent galaxy (Tremonti et al. 2004).

Resolved kinematic studies of UCDs are only feasible for the brightest UCDs, and thus our existing sample is strongly biased toward more massive UCDs ($> 10^7 M_\odot$), while in fact there are many more UCDs at lower masses. There is no measurement of the presence of SMBHs in lower mass UCDs yet, and the incidence of genuine nuclei is entirely unknown for low-mass UCDs. If stripped nuclei exist among low-mass UCDs, they most likely originate from low-mass ($\sim 1 \times 10^9 M_\odot$) parent galaxies. For this mass range, the BH demographics are not well known, but even these low-mass nuclei appear to host BHs (Miller et al. 2015; Nguyen et al. 2017). To provide a first look inside lower mass UCDs, we target two UCDs below $10^7 M_\odot$ in this work to explore whether they also host SMBHs in their centers. Owing to their lower brightness, the required adaptive optics observations are only feasible for UCDs that are closer than the Fornax or Virgo clusters.

We chose to target two Centaurus A UCDs (UCD 320 and UCD 330, also named HGHH92-C21 and HGHH92-C23, respectively; see Taylor et al. 2010; Rejkuba et al. 2007 for reference) that are both more massive than ω Cen. We show below that the masses are $2.8 \times 10^6 M_\odot$ and $6.1 \times 10^6 M_\odot$ for UCD 320 and UCD 330, respectively, and their other properties are summarized in Table 1.

Both objects have dynamical mass-to-light ratios (M/L_{dyn}) that are higher than what is expected from stellar population predictions (M/L_{pop}). Based on the SMBHs found in massive UCDs, this inflated M/L may be a sign of massive BHs in these systems (Ahn et al. 2017). The enhancement for UCD 320 was $\Psi_{330} = \frac{M/L_{\text{dyn}}}{M/L_{\text{pop}}} = 2.28$ and $\Psi_{320} = \frac{M/L_{\text{dyn}}}{M/L_{\text{pop}}} = 2.5$ for UCD 330.

These observations are part of an adaptive optics campaign that uses the VLT/SINFONI (PI: Mieske) and for the UCDs in the northern hemisphere with Gemini/NIFS (PI: Seth). Both UCDs have been first noted in Harris et al. (1992), and their integrated velocity dispersion was measured in Rejkuba et al.

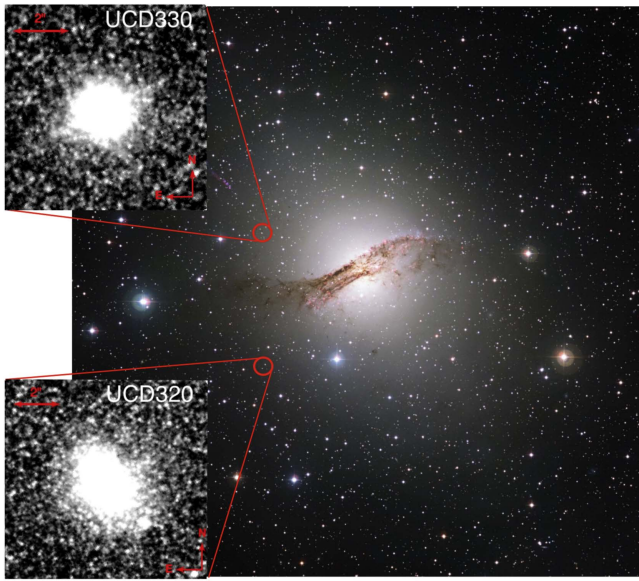


Figure 1. Cutout of the *HST* imaging of UCD 330 (top panel) and UCD 320 (bottom panel) with respect to their position within Cen A. UCD 330 lies at a distance of 5.8 kpc to the center of Cen A, and UCD 320 is located at 7.3 kpc. The image of Cen A is a publicly available composite image taken from ESO (<https://www.eso.org/public/images/eso1221a/>).

(2007). The data of Rejkuba et al. (2007) were reanalyzed by Taylor et al. (2010).

In the paper we adopt a distance modulus of $m-M = 27.91$ to Cen A (Harris et al. 2010) and an extinction value of $A_V = 0.31$ mag.

This paper is organized in the following way: In Section 2 we present our data and how they were analyzed. In Section 3.1 we present our methods for measuring the kinematics and the mass and surface-brightness profile of the UCD and the set-up of the Jeans Anisotropic Models (JAM). In Section 4 we present our results from the kinematic measurements and in Section 5 the results from the dynamical modeling. In Section 6 we discuss our findings, and in Section 7 we present the conclusion.

2. Data

2.1. SINFONI Observations

UCD 320 and UCD 330 were observed with SINFONI (Eisenhauer et al. 2003) on UT4 of the Very Large Telescope (VLT), under ESO ID Nr.095.B-0451(A) (PI: Mieske). SINFONI is a near-infrared integral field spectrograph with adaptive optics capabilities. All our observations were carried out in the K band ($1.95\text{--}2.45\ \mu\text{m}$) with a pixel scale of $50 \times 100\text{ mas}$, a field of view of $3'' \times 3''$, and a spectral resolution of $R \sim 4000$.

In total, 21 exposures of 600 s were combined into the final cube for UCD 330. The observations were carried out on the nights of 2015 June 15, 18, 21, and 24th.

For UCD 320, we observed 28 exposures of 600 s and had to discard 6 of them because of low quality, where the adaptive optics loop was not stable. For the final cube, we combined 22 exposures. The data were reduced using version 3.12.3 of the esorex command-line software and version 1.8.2 of the SINFONI instrument pipeline. We corrected each individual observation with the dark exposure and applied the pipeline recipes that correct linearity and distortion. We then divided

by the flat field, applied a wavelength correction, and corrected for the telluric absorption features. The sky was subtracted using the two offset sky exposures taken in each observing block in an O-S-O-S-O sequence, with offsets of $4''$ and $7''$ from the center of the UCD. The individual cubes were dithered in such a way that the object fell for half of the total exposure time onto the lower right part of the detector and the other half on the upper left part. Additionally, a dither of a few pixels was applied between successive exposures at both positions, to ensure that the UCDs did not fall into the same area of the detector each time. This ensures that systematic detector effects are minimized and that unique sky pixels are subtracted from each dither position. The individual cubes were combined using our own routine that centers on each UCD and coadds them so that they are aligned.

Despite the sky subtraction, the reduced cubes still had significant background flux left in the spectra. This residual background was uniform in spectral distribution across the chip, but had neither the spectrum expected for a stellar source, nor sky emission. We suspect the background is due to scattered light, similar to backgrounds seen in comparable SINFONI data (Nguyen et al. 2017). We estimated the background spectrum using the spatial pixels farthest from the center of the UCD, averaged these pixels using sigma clipping, and subtracted this background spectrum from each spatial pixel in the cube. This background correction resulted in significantly improved kinematic fits, but has the consequence of introducing uncertainty into our point-spread function (PSF; see below).

The intrinsic dispersion of SINFONI varies for each row of the 64×64 pixel detector, and thus we need to obtain accurate instrumental dispersion for each row separately. To achieve this, we use five strong OH sky lines with small wavelength separations between the doublets from the sky cubes. For each line, we subtract the continuum, normalize the flux in each line, and then sum over all lines and take their median. Thus we use the empirically determined median line shape of each row as the instrumental dispersion of SINFONI. The line-spread function (LSF) of SINFONI varies significantly from row to row, with FWHMs ranging from 5.7 up to $8.5\ \text{\AA}$. We then dither the LSF cube of the SINFONI field of view in the same manner in which our observations were dithered to create a final combined LSF cube.

We derive the spatial PSF of the SINFONI adaptive optics data by convolving the images from the *Hubble Space Telescope* (*HST*; see Section 2.2) of the UCDs with a model PSF and comparing it to the collapsed image from the SINFONI cubes. For the model PSF, we use a double-Gaussian functional form. The double-Gaussian model parameters are varied until a best-fit convolved *HST* image is found that is closest to the observed SINFONI data.

The additional background subtraction we applied to the SINFONI cube reduced the light in the outskirts relative to the true distribution, potentially impacting our PSF measurement. To measure the accurate surface brightness profile, we needed to quantify what fraction of the signal in the outskirts comes from the UCD (and potentially galaxy) light. We extracted 14 background aperture spectra (using four-pixel apertures) at large radii ($>1, 8''$) from UCD 330. We then compared the $2.3\ \mu\text{m}$ CO-bandhead equivalent widths (EWs) of the background spectra to one from the center of the UCD. No clear CO lines were visible in the background spectra, and from the

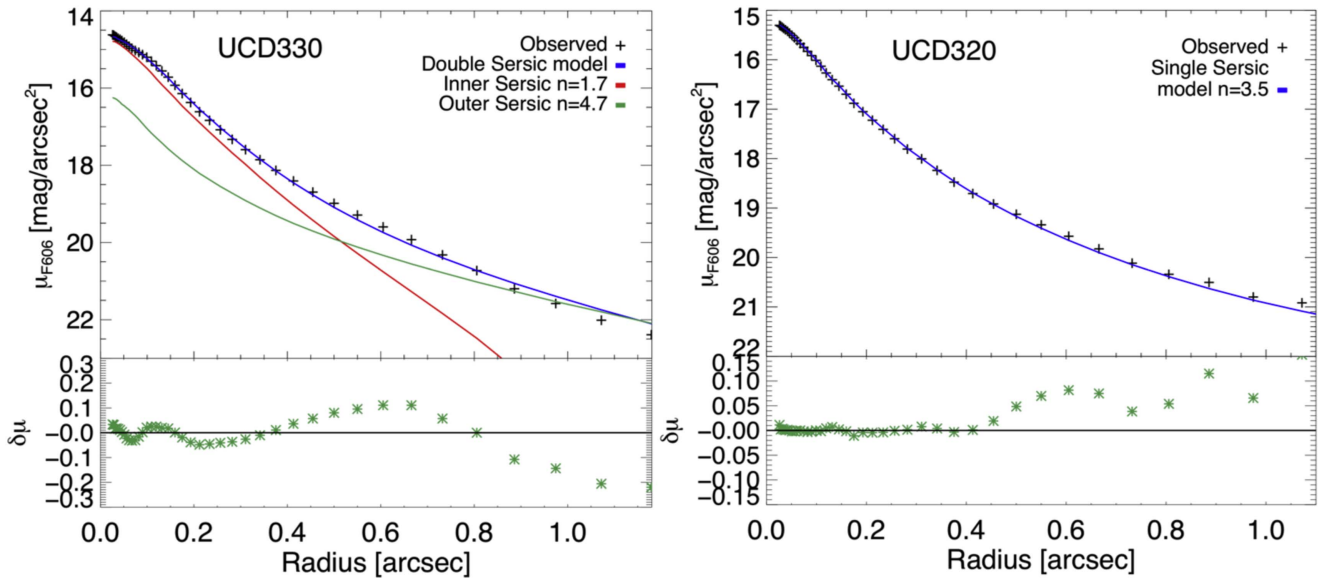


Figure 2. Observed surface brightness profiles of UCD 330 (left) and UCD 320 (right), shown as black pluses. The best-fit double Sérsic model for UCD 330 is shown as a blue line in the left panel and the single Sérsic model for UCD 320 in blue in the right panel. For UCD 330, the inner and outer Sérsic components are shown separately in red and green, respectively. These are the models that were convolved with the PSF from the *HST* images. The individual Sérsic parameters can be found in Table 2.

Table 2
GALFIT Results

Name	Mag (F606W)	R_{eff} (arcsecond)	R_{eff} (pc)	Sérsic Index n	Axis Ratio	P.A.	Reduced χ^2
UCD 330 Inner Sérsic	17.17	0.13	2.17	1.70	0.84	−48.84	4.01
UCD 330 Outer Sérsic	17.72	0.54	8.97	4.73	0.80	−48.69	4.01
UCD 330 Single Sérsic	16.80	0.17	3.11	1.92	0.81	−32.66	6.92
UCD 320 Sérsic	17.30	0.28	4.67	3.46	0.65	−79.82	10.36

Note. The apparent magnitude is corrected for $A_V = 0.31$ mag of extinction.

equivalent width comparison, we deduced that the contribution of a UCD-like spectrum to the background is $10.5\% \pm 7.7\%$ at a radius of $\sim 2''.3$. Because the background spectra have strong structure in wavelength (i.e., it looks like an emission line spectrum), one way to estimate the true surface brightness of the UCD is to make an image out of a region without strong emission in the background spectra. To determine the PSF, we therefore created an image by collapsing the data cube over wavelengths from 2.26 to $2.36 \mu\text{m}$, and then removed $89.5 \pm 7.7\%$ of the background level at $2''.3$ to ensure that the scattered light from the UCD remains. The final PSF for UCD 330 has a inner Gaussian width of $0''.07$, containing 72.9% of the total luminosity, and an outer component of $1''.15$ that contains 27.1% of the light. Considering the uncertainties in the kinematic PSF light contribution, we determined the following values for the outer Gaussian component: $r = 0''.97$ with a 20.5% light fraction as a lower limit, and $r = 1''.34$ with a 35% light fraction as the upper limit. The size of the inner component remained the same in both fits.

For UCD 320, this method results in a FWHM of $0''.16$ for the inner Gaussian, containing 59.8% of the light, and the outer component has a size of $0''.85$ and a light fraction of 40.2%. Using the equivalent width method, we find a UCD light contribution of $9\% \pm 6\%$. The change in UCD light contribution varied the light fraction in the outer Gaussian only by a

small amount, with $40^{+3}_{-2}\%$. The sizes of the inner and outer Gaussian were essentially unchanged.

2.2. HST Data

High-resolution imaging data from *HST* were available in the Hubble Legacy Archive¹³ for both UCDs. The available imaging data were taken with the Wide Field Camera (WFC) on the Advanced Camera for Surveys (ACS) using the F606W filter. The combination of ACS/WFC provides a spatial resolution of $0''.05 \text{ pix}^{-1}$. UCD 320 and UCD 330 were observed as part of *HST* Proposal 10597 (PI: Jordan) that targeted the structural parameters of GCs around Cen A. The total observing time was 2158 s. We note that due to the single band of data, we cannot study color variations within the UCD or variations that would affect our assumption of a constant M/L , but as shown in Ahn et al. (2017), these variations, even if present, have minimal effects on the dynamical models.

The images are available in their fully reduced form from the *HST* archive. We used them to analyze the surface-brightness profile of the UCDs and determine their structural parameters. These spatially resolved light profiles are an important ingredient for the dynamical models of our UCDs. A cutout of the *HST* images and the position of the UCDs within CenA is illustrated in Figure 1.

¹³ <https://hla.stsci.edu/>

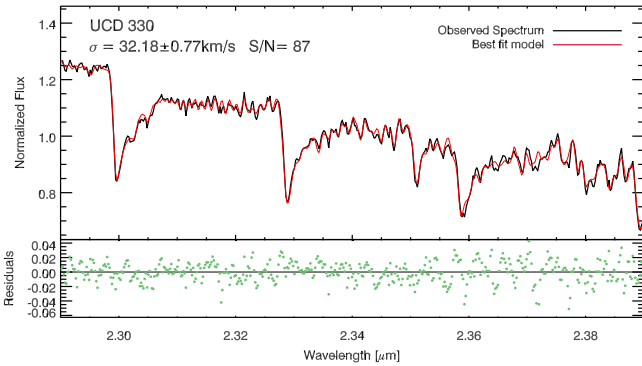


Figure 3. Near-infrared spectrum of UCD 330 centered on the CO-bandhead absorption features between 2.29 and 2.39 μm . The spectrum was integrated out to $0''.4$ in radial distance. The observed spectrum is shown in black, the best-fit model is plotted in red, and the residuals are shown in the panel below in green.

The PSF was generated empirically using isolated point sources in *HST* images taken with similar dither patterns. These stars were combined into a single image, and a spatially varying PSF was determined using the Fortran version of DAOPHOT.

3. Analysis

3.1. Kinematics Measurements

For our dynamical analysis, we use the strong near-infrared CO band absorption lines from 2.29 to 2.39 μm , which are located in the *K* band that we observed with SINFONI. To fit stellar templates to the absorption lines, we use the penalized pixel-fitting (pPXF) code (Cappellari & Emsellem 2004; Cappellari 2017). It allows one to fit a set of model templates to the data and derives the best-fit radial velocity and velocity dispersion of the observed spectrum. For our stellar model spectra, we use the library of high-resolution stellar templates of cool stars in the *K* band from Wallace & Hinkle (1996). The high-resolution model spectra are convolved with the SINFONI line-spread function to bring them to the same spectral resolution as our UCD observations.

For UCD 330, the signal-to-noise ratio (S/N) was sufficient to create 2D kinematic maps using Voroni binning (Cappellari & Copin 2003). We required that each bin has a minimum $\text{S/N} > 30$. Outside of $r > 0''.3$, we created bins that spanned 90° intervals to maximize the S/N. However, for the significantly lower S/N of UCD 320, we needed to restrict our analysis to (1D) radial binning.

We did not fit the *h3* (skewness) and *h4* (kurtosis) parameters, as the spectra did not have the necessary S/N to draw reliable conclusions about the shape of our absorption lines. Before carrying out the kinematic fits, we coadded several spaxels into bins to improve the S/N. For the radial dispersion profiles of both UCDs, we summed all pixels in radial bins.

The uncertainties of our kinematic measurements were determined by adding random Gaussian noise to our spectra. The random noise level is based on the residual from the best-fit model. We ran such Monte Carlo simulations 25 times for each spectrum and refitted the kinematics. The standard deviation of the kinematic values from the 25 trials was then adopted as the 1σ kinematic error.

We performed a barycentric velocity correction for all measured radial velocities. We used the barycentric correction

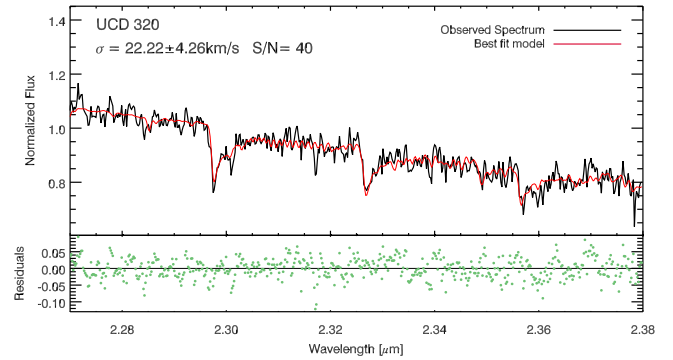


Figure 4. Integrated *K_s*-band spectrum of UCD 320 with the CO-bandhead absorption features plotted between 2.27 and 2.38 μm . The spectrum was integrated out to $0''.3$ in radial distance to optimize the S/N that decreases when coadding more distant spaxels that are noisier because of the decreasing flux of the object. The observed spectrum is plotted in black, the best-fit model is shown in red, and the residuals are plotted in the panel below.

at the date of observation for each individual exposure, and then averaged all corrections. For UCD 330, the average correction is $v_{\text{bary}} = -19.1 \text{ km s}^{-1}$, and for UCD 320, it is $v_{\text{bary}} = -21.9 \text{ km s}^{-1}$.

3.2. Surface Brightness and Mass Profiles

Every JAM model requires a model for the distribution of the stellar mass within the UCD. We can derive the surface brightness profile of our UCDs from the available *HST* images in the F606W filter. We use the 2D surface brightness code GALFIT (Peng et al. 2002) to fit a double Sérsic light profile. We fit both UCDs using a $10'' \times 10''$ cutout of the *HST* F606W imaging (Figure 1) with an 80×80 pixel PSF convolution box. The best-fit model parameters of the Sérsic profiles are listed in Table 2. We first ran a single Sérsic profile to measure the best-fit center of the UCD. Then we refit a double Sérsic profile, assuming the same center for both Sérsic components and keeping it fixed. The other fit parameters, including the magnitude, effective radius, Sérsic index, ellipticity, and position angle, were all allowed to vary for both UCDs. We also allowed GALFIT to account for a background gradient to take into account the varying background light from Cen A. For UCD 320, the single Sérsic fit was the best-fit model, whereas for UCD 330, the double Sérsic fits had a lower reduced χ^2 value than the single-component model.

For UCD 330, we find a best-fit inner component with $r_{\text{inner}} = 0''.13 = 2.4 \text{ pc}$ and a Sérsic index of $n = 1.7$, and $r_{\text{outer}} = 0''.54 = 9.97 \text{ pc}$ and $n = 4.73$ for the outer component. With axis ratios of 0.84 and 0.80, respectively, the two components are similar in ellipticity. The combined effective radius of these two components is $r_{\text{eff}} = 0''.2 = 3.69 \text{ pc}$, which is larger than the literature value (Table 1). The total extinction-corrected F606W magnitude is $m_{\text{F606}} = 16.66$, which translates into $m_V = 16.88$. Thus the absolute magnitude is $M_V = -11.03$. Rejkuba et al. (2007) find $M_V = -11.66$ after applying an 0.64 mag internal extinction correction for dust in Cen A, in addition to their external 0.34 mag foreground extinction correction. When we only correct for the foreground extinction, the magnitude is $M_V = -11.02$, which is consistent with our value. This is the only object for which Rejkuba et al. (2007) applied this additional correction based on the presence of strong NaD lines. However, the lines themselves are too noisy to measure the internal extinction directly, and thus their

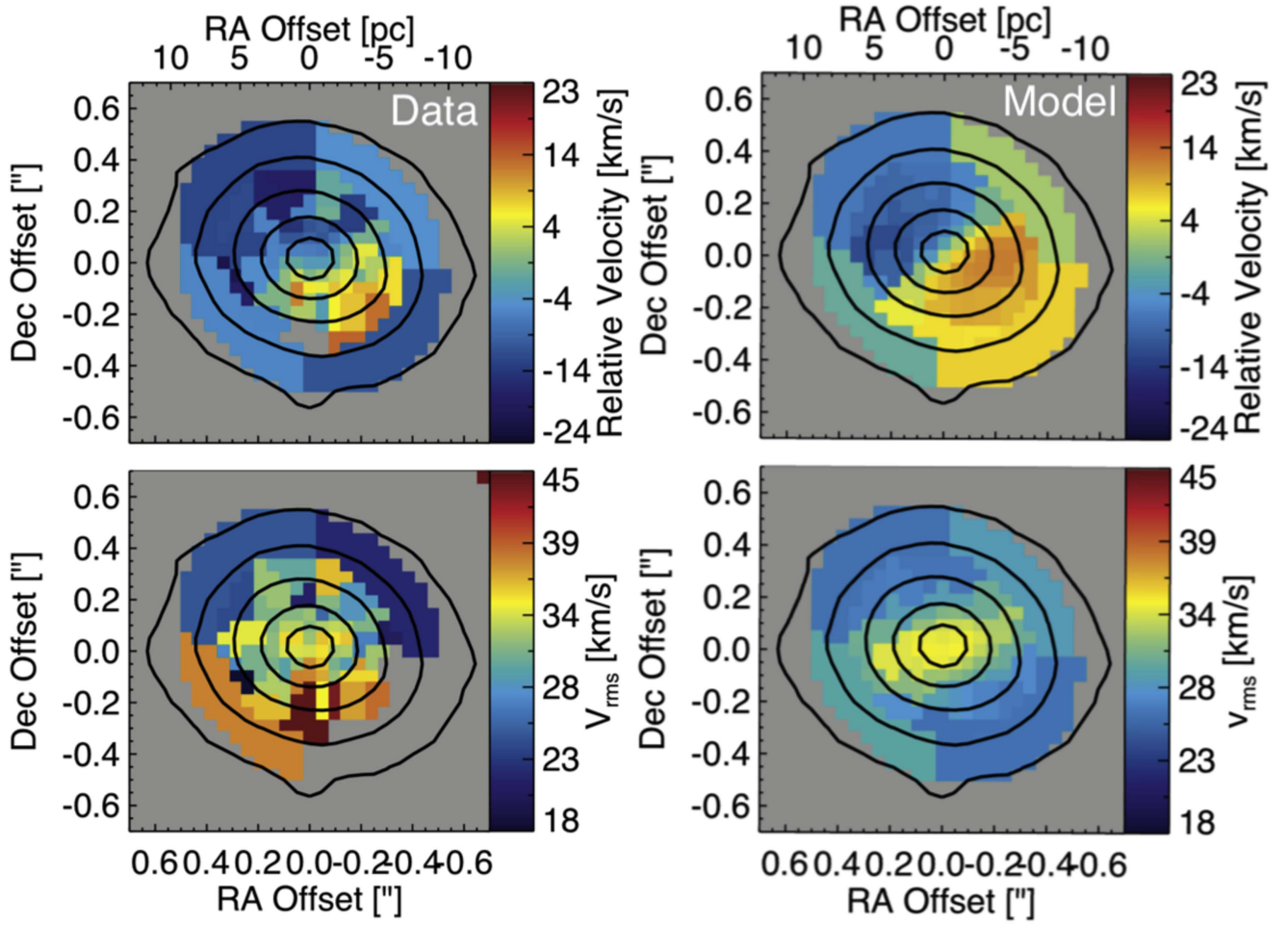


Figure 5. Two-dimensional kinematic maps (left) and models (right) of UCD 330. The top panels show the radial velocities, and the bottom panels show the second moment of the LOSVD $v_{\text{rms}} = \sqrt{\sigma^2 + v_{\text{rad}}^2}$ that includes the velocity dispersion and the radial velocity. The black isophotes show the contours of the stellar light from the K -band image. For the central area, the S/N is high enough that the dynamics were measured for single pixels, whereas in the outskirts, many pixels were binned together. The typical uncertainties for the v_{rms} are 2 km s^{-1} for the central pixels and 6 km s^{-1} in the outskirts. Grayed-out bins in the data panels are either bins with an S/N < 5, or the uncertainties on the dispersion and radial velocity are above 15 km s^{-1} .

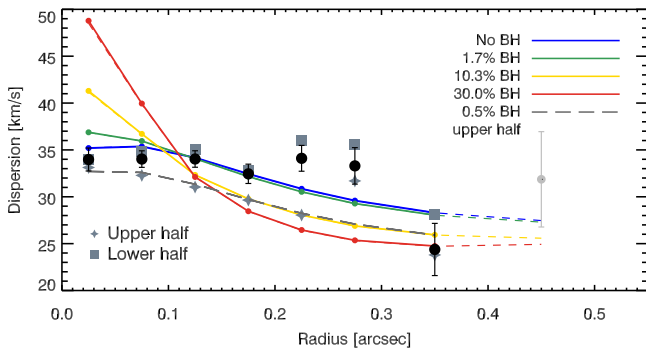


Figure 6. Black points are the measured radial dispersion profile of UCD 330. The colored lines are the best-fit isotropic models with increasing BH mass, the dashed colored lines are the models extended to the region where we did not fit them. The zero-mass BH model (blue) is the best overall model, and the model with 1.7% BH mass fraction (green) is the 3σ upper limit. The BH fractions of 1.7%, 10.3%, and 30.0% correspond to absolute BH masses of 1.0×10^5 , 4.6×10^5 , $1.0 \times 10^6 M_{\odot}$. The light gray data point of the outermost bin was not included in the JAM modeling. The dark gray squares and stars are the radial dispersion profile of the lower and upper half of the UCD, respectively. The dashed gray line is the best-fit upper-half model containing a BH of $2.14 \times 10^4 M_{\odot}$, corresponding to a BH fraction of 0.5%.

internal extinction value is an estimate. In addition, the extinction-corrected $(V - I)$ color of UCD 330 is 0.78 in Rejkuba et al. (2007), but for a 12.6 Gyr old stellar population with a cluster metallicity of $[\text{Fe}/\text{H}] = -0.4$, the Padova models predict a $(V - I) = 1.15$ (Girardi et al. 2000); when correcting only for the foreground extinction, this matches much better: it yields a $V - I = 1.11$ for UCD 330. This suggests that their large internal extinction correction is overestimated, and thus we do not apply it.

For UCD 320, we find the best-fit profile to be a single Sérsic with $r_{\text{eff}} = 0''.28 = 5.17 \text{ pc}$, a Sérsic index of $n = 3.46$, and an axis ratio of 0.65. Thus UCD 320 is significantly elliptical and smaller than the previous effective radius of 6.83 pc (Table 1). Its extinction-corrected F606W magnitude is $m_{\text{F606}} = 17.30$, which translates into $m_V = 17.52$, and thus the absolute magnitude is $M_V = -10.39$, which is exactly the same value as was found in the literature and is also corrected for foreground Milky Way extinction (see Table 1).

The surface brightness profiles of the two UCDs and their best-fit Sérsic models derived with GALFIT are shown in Figure 2. The black pluses show the measured values, and the blue line presents the best-fit model that was convolved with the PSF.

Table 3

Radial Velocities and Velocity Dispersion of UCD 330 and 320 and the S/N of Each Radial Bin

Radius (arcsec)	Radius (pc)	Velocity v_r (km s ⁻¹)	Dispersion σ_v (km s ⁻¹)	S/N
UCD 330				
0.025	0.42	735.8 ± 0.90	33.98 ± 0.84	83.8
0.075	1.25	737.8 ± 0.74	34.02 ± 0.73	104.3
0.125	2.08	739.8 ± 0.75	34.03 ± 0.75	102.0
0.175	2.91	741.8 ± 0.92	32.45 ± 1.01	79.9
0.225	3.74	741.7 ± 1.46	34.10 ± 1.41	56.8
0.275	4.57	738.8 ± 1.93	33.30 ± 2.08	42.0
0.350	5.81	736.9 ± 2.32	24.38 ± 2.92	29.2
0.450	7.48	742.7 ± 4.96	31.86 ± 5.78	17.9
UCD 320				
0.025	0.42	500.8 ± 5.3	29.52 ± 11.57	28.50
0.075	1.25	498.2 ± 3.3	21.05 ± 5.22	36.03
0.125	2.08	497.9 ± 3.7	20.64 ± 4.46	33.29
0.175	2.91	500.5 ± 3.4	21.69 ± 4.37	34.46
0.250	4.15	505.5 ± 5.0	22.82 ± 7.52	23.76

Table 4

Summary of the Measured Values and Limits for UCD 330 and UCD 320

	UCD 330	UCD 320
M_V	-11.03	-10.39
$M_{\text{tot}} [M_\odot]$	$6.10 \pm 0.23 \times 10^6$	$2.81^{+2.5}_{-1.3} \times 10^6$
$\Psi = M_{\text{dyn}}/M_{\text{pop}}$	$0.90^{+0.3}_{-0.6}$	$0.94^{+0.8}_{-0.5}$
M/L_{F606}	$2.65^{+0.15}_{-0.55}$	$2.20^{+1.9}_{-1.0}$
M/L_V	$2.97^{+0.17}_{-0.50}$	$2.47^{+2.1}_{-1.0}$
β_z	$0.0^{+0.2}_{-0.4}$	$-0.2^{+0.6}_{-0.4}$
3σ upper limit: $M_\bullet [M_\odot]$	1.0×10^5	1.0×10^6
3σ upper limit $M_\bullet/M_{\text{tot}} [\%]$	1.7	37.7

We use the multi-Gaussian expansion (MGE) code (Cappellari 2002) to parametrize the UCD surface brightness profiles using several 2D Gaussian models. The final 2D surface brightness model of the UCDs can then be analytically deprojected into a 3D model. The MGE surface brightness profiles (in units of L_\odot/pc^2) are given in Tables 5 and 6, respectively. Assuming a constant mass-to-light ratio for the stellar population means that the surface brightness profile directly translates into the stellar mass profile.

3.3. Jeans Anisotropic Models

We model our UCDs using the JAM code (Cappellari 2008), which predicts the kinematics of an axisymmetric stellar system based on a supplied luminosity profile. This is compared to kinematic data to constrain the free parameters such as the M/L , BH mass, and orbital anisotropy. This code provides both the radial velocity and velocity dispersion parameters as model outputs. In a cylindrical coordinate system where the z -axis is aligned with the object's symmetry axis, the anisotropy is defined as $\beta_z = 1 - (\frac{\sigma_z}{\sigma_r})^2$.

In addition to the stellar mass profile, the JAM code adds a Gaussian mass profile to model the presence of a central black hole. The JAM models predict the $\sigma_{\text{rms}} = \sqrt{v_{\text{rad}}^2 + \sigma^2}$ profile, and thus cannot be compared to the full line-of-sight (LOS)

Table 5

Multi-Gaussian Expansion of UCD 330 that Provides the Luminosity Model for the JAM Code. The Horizontal Line Separates the Two Components of the Sérsic Model

Luminosity $\frac{L_\odot}{\text{pc}^2}$	σ "	q	Position Angle °
50415.66	0.0012	0.841	-48.84
71147.24	0.0040	0.841	-48.84
81974.73	0.01078	0.841	-48.84
74298.20	0.0251	0.841	-48.84
50359.54	0.0516	0.841	-48.84
24333.01	0.0962	0.841	-48.84
7999.0797	0.1651	0.841	-48.84
1718.68	0.2651	0.841	-48.84
229.46	0.4079	0.841	-48.84
12.88	0.6372	0.841	-48.84
244219.16	0.0004	0.8000	-48.69
174900.37	0.0010	0.8000	-48.69
117329.34	0.0025	0.8000	-48.69
72208.21	0.0061	0.8000	-48.69
39796.08	0.0140	0.8000	-48.69
19754.61	0.0309	0.8000	-48.69
8705.59	0.0657	0.8000	-48.69
3384.10	0.1350	0.8000	-48.69
1151.80	0.2690	0.8000	-48.69
337.71	0.5191	0.8000	-48.69
87.01	0.9691	0.8000	-48.69
19.30	1.7639	0.8000	-48.69
3.63	3.1265	0.8000	-48.69
0.59	5.4029	0.8000	-48.69
0.08	9.1426	0.8000	-48.69
0.01	15.4174	0.8000	-48.69
0.001	28.2834	0.8000	-48.69

Table 6

Multi-Gaussian Expansion of UCD 320 that Provides the Luminosity Model for the JAM Code

Luminosity $\frac{L_\odot}{\text{pc}^2}$	σ "	q	Position Angle °
297084.18	0.0005	0.646	-79.79
256401.63	0.0012	0.646	-79.79
200800.78	0.0031	0.646	-79.79
140971.31	0.0073	0.646	-79.79
88486.19	0.0162	0.646	-79.79
48435.90	0.0346	0.646	-79.79
22142.39	0.0705	0.646	-79.79
8633.37	0.1367	0.646	-79.79
2894.15	0.2541	0.646	-79.79
795.18	0.4570	0.646	-79.79
179.44	0.7942	0.646	-79.79
32.91	1.3367	0.646	-79.79
4.95	2.1895	0.646	-79.79
0.58	3.5684	0.646	-79.79
0.04	6.2344	0.646	-79.79

velocity distribution, as more sophisticated orbit-based models, such as Schwarzschild models, can. Similar to the gravitational effect of a black hole, radial anisotropy increases the dispersion near the center. Thus the black hole mass and anisotropy are intrinsically degenerate with each other. We can explore the effects of the degeneracy using grids with a range of anisotropies and BH masses.

For UCD 330 and UCD 320, we run a grid of JAM models with four free parameters: black-hole mass M_* , anisotropy β_z , mass-to-light ratio M/L_{F606W} , and the inclination. We use the following grid:

1. Ten values for the BH mass, including a zero-mass BH and 9 BH masses ranging from $\log(M_*/M_\odot) = 4-6.66$ in increments of $\log(M_*/M_\odot) = 0.33$.
2. Thirty values for M/L_{F606W} ranging from 0.55 to 4.9 in steps of 0.15
3. Ten anisotropies β_z ranging from -1.0 to 0.8 in increments of 0.2
4. Six inclinations ranging from 40° to 90° in increments of 10°

In the remaining paper, we do not report the M/L_{F606W} values directly, but rather the quantity $\Psi = \frac{M/L_{F606W}}{M/L_{\text{pop}}}$, which is the dynamical mass-to-light ratio normalized with the predicted M/L ratio from stellar population models.

The predicted M/L_{pop} ratios are calculated similar to Mieske et al. (2013), using the average of the Maraston (2005) and the Bruzual & Charlot (2003) stellar population models for an object of 13 Gyr using the mean of a Kroupa and Chabrier initial mass function (IMF). We assume $[\text{Fe}/\text{H}] = -0.36 \pm 0.14$ for UCD 330 and $[\text{Fe}/\text{H}] = -0.85 \pm 0.14$ for UCD 320, taken from Beasley et al. (2008). Using these metallicities, the predicted M/L_{pop} values are $M/L_{\text{pop},V} = 3.30$ and $M/L_{\text{pop},V} = 2.64$ for UCD 330 and UCD 320, respectively. We translate this into the F606W band predictions by adopting a $V\text{-F606W} = 0.219$ mag color difference between the V band and the HST F606W filter and a 0.1 mag color difference of the Sun. The F606W predictions are then $M/L_{\text{pop},F606W} = 2.95 \pm 0.22$ for UCD 330 and $M/L_{\text{pop},F606W} = 2.37 \pm 0.13$ for UCD 320. The uncertainties on the M/L_{pop} predictions are derived from propagating the 0.14 dex error of the metallicity measurement (Beasley et al. 2008) into the stellar population prediction.

We used the same grid of JAM models on both UCDs. For each UCD, we derived likelihood maps that show the degeneracy between two of the fit parameters each. For this, we marginalized the grid over the two parameters that are not plotted. We used the reduced χ^2 value of each model to calculate the likelihood for each point in the grid where we evaluated a model. We then used these likelihood values and plotted the contours of the 1, 2, and 3σ levels. The modeling results and likelihood maps are shown in Section 5.

4. Kinematic Results

4.1. Integrated Velocity Dispersions

First, we coadd the spectra within a circular aperture of $0''.4$ for UCD 330 and $0''.3$ for UCD 320 to obtain an integrated spectrum. Using the pPXF code, we fit stellar templates to the observed spectra (see Section 3.1) to derive their velocity dispersion.

For UCD 330, the mean S/N of 87 enables an accurate determination of the integrated velocity dispersion. We find a dispersion of $\sigma_v = 32.18 \pm 0.77 \text{ km s}^{-1}$ (see Figure 3). In comparison, the integrated dispersion value of $\sigma_v = 30.9 \pm 1.5 \text{ km s}^{-1}$ in Rejkuba et al. (2007) was determined from high-resolution UVES data in a $1''$ aperture. To correct for the larger aperture, we use the JAM models with a pixel size set to $1''$ to predict the integrated dispersion of UCD 330 for a similar aperture.

We predict a dispersion of $\sigma_v = 30.79 \text{ km s}^{-1}$ in the larger aperture, which is fully consistent within the error bars with the values of Rejkuba et al. (2007).

For UCD 320, we performed a similar analysis, but included the bluer parts of the spectra down to $\lambda = 2.20 \mu\text{m}$ in our fits to improve the S/N. With this, we were able to reach a median S/N of 40 per pixel when integrating out to $0''.3$, which is plotted in Figure 4. Coadding spectra from spaxels at larger distances does not add to the S/N but rather decreases it. We find an integrated dispersion of $\sigma_v = 22.22 \pm 4.26 \text{ km s}^{-1}$. Owing to the lower S/N for this UCD, the measurement has a higher uncertainty. We also predict the integrated dispersion using a $1''$ aperture for UCD 320. We predict a dispersion of $\sigma_v = 19.70 \text{ km s}^{-1}$, which is fully consistent with the $\sigma_v = 20.9 \pm 1.6 \text{ km s}^{-1}$ value derived by Rejkuba et al. (2007) and the $\sigma_v = 20.0 \pm 1.4 \text{ km s}^{-1}$ measured in Taylor et al. (2010). The fact that our integrated dispersion is consistent with their value indicates that we can reliably measure velocity dispersions of $\sim 20 \text{ km s}^{-1}$ close to the SINFONI resolution limit.

Taylor et al. (2010) reanalyzed the high-resolution UVES data for UCD 330 from Rejkuba et al. (2007) and found a dispersion of $\sigma_v = 41.5 \pm 3.7 \text{ km s}^{-1}$, which is a $\sim 2.5\sigma$ outlier from the integrated dispersions found in Rejkuba et al. (2007) and in this work. A new measurement of $\sigma_v = 29.2 \pm 3.0 \text{ km s}^{-1}$ of the UCD 330 dispersion from Hernandez et al. (2018) is also consistent with our measurement.

As our dispersion, the original measurement from Rejkuba et al. (2007), and the independent one of Hernandez et al. (2018) agree with each other, it is likely that the Taylor et al. (2010) value is the outlier. We note that this high dispersion resulted in Taylor et al. (2010) measuring a dynamical M/L more than twice as high as what was expected. We revisit this after deriving our best-fit M/L s below.

4.2. Two-dimensional Resolved Kinematic Map of UCD 330

The high quality of the UCD 330 data permits us to measure a resolved 2D kinematic map. The results of the kinematic measurements are shown in the two left panels of Figure 5. The map of the radial velocity is shown in the top left panel, and the map of the second order momenta $v_{\text{rms}} = \sqrt{v_{\text{rad}}^2 + \sigma^2}$ is shown in the bottom left panel. The best-fit JAM model is shown in the two panels on the right, and we discuss its results in Section 5. The typical uncertainties on the v_{rms} are 2 km s^{-1} for the central individual pixel bins and $\sim 6 \text{ km s}^{-1}$ in the outer larger bins.

The observed velocity map is normalized to the systemic velocity of UCD 330 of $v_{\text{sys}} = 743 \text{ km s}^{-1}$. The amplitude of the observed rotation is $\sim 12 \text{ km s}^{-1}$, with the rotation axis aligned with the semiminor axis of the UCD. The fraction of rotational versus dispersion support in this UCD is $v_{\text{rot}}/\sigma = 0.37$ when compared to the global velocity dispersion. This indicates a significant contribution from rotation. With an average axis ratio of 0.82 for UCD 330, we would expect $v_{\text{rot}}/\sigma = 0.4$ (Binney 1978) from a self-gravitating system that is flattened by its rotational support, which is consistent with what we observe.

The observed v_{rms} map in the bottom left panel of Figure 5 is more complex. In the top half of the map, the dispersion in the outskirts is $\sim 20 \text{ km s}^{-1}$ and increases toward values of $\sigma = 34 \text{ km s}^{-1}$ in the center, with observational noise adding some

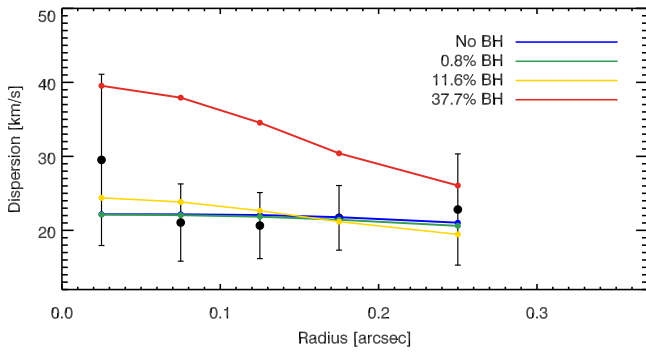


Figure 7. Black points are the measured radial dispersion profile of UCD 320. The colored lines are models with increasing BH mass. The 0.8% BH model (green) is the best overall model, and the 37.7% model (red) is the 3σ upper limit. The BH fractions of 0.8%, 11.6%, and 37.7% correspond to absolute BH masses of 2.15×10^4 , 2.15×10^5 , and $1 \times 10^6 M_\odot$.

scatter. However, the top half of the dispersion map is overall consistent with a radially decreasing velocity dispersion profile.

The velocity dispersion at the bottom of the v_{rms} map appears unusual, with several high-dispersion outer bins. An asymmetric dispersion profile is highly unusual as the dispersion is expected to decrease outward at all angles. It is unclear what could cause such a high-dispersion region. We tested whether it might be a detector issue by analyzing the individual cubes separately and checking if the results are consistent. We did not find a significant difference between the kinematic results for individual cubes. As our individual cubes are dithered by significant amounts so that in each individual cube the UCD is at a different detector location, it is unlikely to be a detector effect. A physical explanation could be that the UCD is semi-resolved into stars and internal bright-star variations causing the elevated dispersion, or that an object in projection contaminates the measurements. Another alternative is that the UCD is tidally disturbed and this increased its dispersion. However, in this case, it would be strange that the disturbances are confined to only one side of the UCD and are not symmetric.

4.3. Radial Dispersion Profiles

In addition to the 2D kinematical map of UCD 330, we also measure the radial dispersion profile. The radial dispersion values can be found in Table 3 and are plotted as black points in Figure 6. For UCD 330, we have data with a high S/N and thus were able to use seven radial bins of $0''.05$ width to measure the kinematics. The S/N for our central bins is between 80 and 100 and decreases to 20–40 in the outskirts. Our measured velocity dispersion errors are small, with 1 km s^{-1} in the center and 2 km s^{-1} in the outskirts.

For UCD 330, the resulting radial dispersion profile in Figure 6 is very flat. The 2D map in the previous section indicates that the increased dispersion values in the UCD come from the increased region at the bottom of the UCD.

To investigate the differences between the “upper” and “lower” part of the UCDs, we split its velocity dispersion profile with a horizontal line crossing the center and remeasured the radial dispersions separately. They are plotted in Figure 6 as gray squares and stars, respectively. Comparing the radial dispersion profiles of both halves has the advantage that we obtain a higher S/N per bin than in the 2D map to test if the high-dispersion areas in the 2D map are significant.

It is apparent from Figure 5 that the flat and even increasing dispersion is mainly caused by the lower half of UCD 330

(gray squares), which is much higher in the outskirts than the dispersion measurements for the upper half (gray stars). These measurements gradually decrease toward the outskirts, with one outlier from this gradual decrease at the $0''.275$ bin.

Considering the statistical significance of the differences between “upper” and “lower” velocity dispersion values, we find that the lower half measurements at $r = 0''.075$, $0''.125$, $0''.175$, and $0''.225$ are discrepant with respect to the measurements of the upper UCD half (gray stars) at 2.5, 3.2, 1.9, and 3.8σ significance. Taken together, it is clear that this enhancement is significant. The flatness of the radial dispersion profile in the outskirts (see Figure 6) is caused mostly by the contribution of the high-dispersion region in the lower half.

The radial dispersion profile of UCD 320 is much less well constrained because of the poorer data quality. We have five radial bins for which we are able to measure the radial velocity and velocity dispersion (see Table 3); this is plotted in Figure 7 as black points. These bins reach an S/N of between 24 and 36. The dispersion profile is flat for the outer four bins, with values around $\sigma_v = 20\text{--}22 \text{ km s}^{-1}$, which is consistent with what we derived for the integrated dispersion. Only the central bin shows an increase in dispersion to almost 30 km s^{-1} , but with the large uncertainty of 11 km s^{-1} , this increase is not statistically significant.

We measure the rotation of UCD 320 by dividing the data at varying position angles and measure the radial velocity for both sides. This is done in intervals of 10° in PA. The resulting amplitude A of the rotation curve is $A = 5.25 \text{ km s}^{-1}$. Taking into account that the rotational velocity varies with the azimuthal angle, we calculate the true rotation velocity using $v_{\text{rot}} = A/\frac{\pi}{4} = 6.68 \text{ km s}^{-1}$. Therefore we derive the rotational versus dispersion support in this UCD as $v_{\text{rot}}/\sigma = 0.3$. For its axis ratio of 0.65, we expect a $v_{\text{rot}}/\sigma = 0.6$ (Binney 1978) from a self-gravitating system that is flattened by its rotational support, which is significantly higher than the measured value, therefore some anisotropy is implied.

5. Dynamical Models

5.1. Two-dimensional JAM Models for UCD 330

We run a large grid of 2D JAM models (Section 3.3) that allow for varying black hole masses, anisotropy, mass-to-light ratios, and inclination angles. The JAM model predictions are used to fit the v_{rms} data shown in Figure 5.

No black hole is detected in UCD 330. The best-fit model has a black hole mass of 0, with a 3σ upper limit of $1.0 \times 10^5 M_\odot$ that equals 1.7% of the best-fit total mass. We quote 3σ errors on all model quantities. The best-fit M/L is 2.65 in the F606W band, which translates into an M/L_V of 2.97. Our best-fit model is isotropic with $\beta_z = 0.0^{+0.2}_{-0.4}$. The best-fit model is shown in Figure 5 along with the data. The central rise in the 2D model up to 35 km s^{-1} is similar to what is observed in the UCD in the upper half. The increased dispersion in the lower half of UCD 330 is not reproduced by our model, whose velocity dispersion decreases with larger radius. In the upper half of the UCD, we reproduce the observed velocity dispersion levels in the outskirts of $\sim 24 \text{ km s}^{-1}$. In addition to the v_{rms} data to which the JAM models were fit, the top panels of Figure 5 also show the velocity field data and predictions from this best-fit model assuming the rotation parameter of $\kappa = 1$ (Cappellari 2008). The observed rotational amplitude of $\sim 12 \text{ km s}^{-1}$, which is

aligned with the semiminor axis of the UCD, is well reproduced in the best-fit JAM model.

We compare the predicted $M/L_{\text{F606Wpop}} = 2.95 \pm 0.22$ to the measured dynamical M/L (Section 3.3) and find a $\Psi = \frac{M/L_{\text{dyn}}}{M/L_{\text{pop}}} = 0.90^{+0.27}_{-0.55}$, meaning that the dynamical mass is similar to the prediction from stellar population models within the error bars. This is significantly lower than the $\Psi_{330} = \frac{M/L_{\text{dyn}}}{M/L_{\text{pop}}} = 2.28$ that was determined previously in Taylor et al. (2010).

We derive a total UCD mass of $M_{\text{tot}} = 6.1 \pm 0.23 \times 10^6 M_{\odot}$. This is significantly lower than the dynamical mass $1.4 \times 10^7 M_{\odot}$ estimated with a single integrated dispersion value by Taylor et al. (2010). This difference is caused by our 10 km s^{-1} lower dispersion value, which agrees with Rejkuba et al. (2007). The 3σ BH limit of $M = 1 \times 10^5 M_{\odot}$, making up 1.7% of the UCD mass, excludes an SMBH of a high mass fraction at high significance.

The 2D likelihood distributions comparing two parameters each are shown as the blue contours in the top panel of Figure 8. Each plot is marginalized over the other parameters that are not plotted. The parameters show minimal covariance, but at the highest allowed BH masses, the best-fit models have $\sim 10\%$ lower M/L s ($\Psi \sim 0.8$) and prefer β_z values of roughly -0.2 . Shown as red contours in Figure 8 are the constraints when fitting only the upper part of the 2D dispersion map. We find a 3σ BH limit of $M_{\bullet} = 2.15 \times 10^5 M_{\odot}$ equal to a 4.3% mass fraction BH. The upper limit on the BH mass is somewhat larger, mostly due to a lower M/L in the 2D upper half models, but generally, the contours are consistent. Our overall conclusions that there is no massive BH in UCD 330. This does not change, regardless of whether we use the upper half or the entire 2D dispersion map, and it indicates that our models are robust.

In the next section, we consider models fit just to the radial profile; they are shown as green contours in Figure 5. These models have wider uncertainties because fewer data points are fit. We therefore adopt the best-fit models to the 2D data and the errors from these fits as our final values. To assess our level of systematic error that is due to the poorly constrained PSF, we also reran the dynamical models with the upper or lower limit on the size and light fraction of the kinematic PSF. The likelihood contours were essentially unchanged, showing that our results are robust to small variations in the kinematic PSF.

5.2. UCD 330 Radial JAM Models

In this section, we discuss JAM models fit to the radial profile of UCD 330 only (black points in Figure 6), as a comparison to the two 2D models from the previous section. We run them over the same grid as detailed in Section 3.3. The best contours for the grid of radial models are shown in green in the top row of Figure 8. The top left panel shows that the best-fit radial model for UCD 330 is tangentially anisotropic with $\beta_z = -0.2$ and the best-fit BH mass is no longer 0, but $M_{\bullet} = 4.64 \times 10^5 M_{\odot}$. The shift toward more tangential anisotropy is the main difference between the radial and the 2D models, but their likelihood contours still overlap. Were we to use only the radial fits, the 3σ upper limit on the BH mass would increase to $M_{\bullet} = 4.64 \times 10^5 M_{\odot}$, equal to 10.3% of the total mass (yellow model, Figure 6). However, the radial model constraints are weaker than those from the

2D model because the 2D models have more data points. Therefore we use the results from the 2D models as our final BH constraints for UCD 330. The increased tangential anisotropy is likely due to the high-dispersion area in the lower sections of the UCD, which are integrated into the radial profile and cause it to be flatter than it would be without that area.

To help visualize our BH mass limits, we compare a set of radial isotropic models with different black hole masses to the radial profile of UCD 330 in Figure 6. This plot shows that the best-fit 2D case without a BH (blue line) fits the 1D data very well. The only significant outliers to that model are the two data points in the outskirts, and they are likely due to the high-dispersion region in the lower parts of the UCD. Excluding the higher dispersion portions of the UCD (the “upper half” data plotted as gray stars in Figure 6), we find particularly good agreement with the shape of a 0.5% BH model (dashed gray line) with a lower M/L value, but the BH mass is consistent with zero within 2σ . The maximum mass BH plotted here is $1 \times 10^6 M_{\odot}$ with a 30% mass fraction, its steep rise in the center is clearly excluded by the data.

5.3. Radial Dynamical Models for UCD 320

For UCD 320, our lower S/N data mean that we cannot construct a 2D map, and instead we only consider the radial dispersion profile. As with UCD 330, we also find no evidence for a BH, but our constraints on the allowed BH mass are much weaker than for UCD 330. We model the UCD 320 radial dispersion data with two sets of models; first we examine the results from a grid that includes the full range of anisotropy, then we look at a comparison of isotropic models to the radial dispersion.

Results from the full grid of JAM models for UCD 320 that include anisotropy are shown in the lower panel of Figure 8. We derive a best-fit black hole mass of $M_{\bullet} = 2.15 \times 10^4 M_{\odot}$, which corresponds to 0.8% of the total UCD mass. The 3σ upper limit of $1 \times 10^6 M_{\odot}$ corresponds to a 37.7% mass fraction. This BH mass limit is independent of the assumed anisotropy in the models. Our best-fit M/L_{F606dyn} is $2.20^{+1.9}_{-1.0}$. From this, we derive a total UCD mass of $M_{\text{tot}} = 2.81^{+2.4}_{-1.3} \times 10^6 M_{\odot}$, and find $\Psi = \frac{M/L_{\text{dyn}}}{M/L_{\text{pop}}} = 0.94^{+0.8}_{-0.5}$ (these are 1σ error bars, including the systematic uncertainty in M/L_{pop} of 0.13), indicating that the dynamical mass of this model is similar to what is predicted from stellar population models. The best-fit anisotropy is $\beta_z = -0.2$ with a 3σ upper limit of $\beta_z = 0.8$, but as visible in Figure 8, the anisotropy is not tightly constrained, and thus no lower limit for β_z can be determined.

For the zero BH mass model, we derive a stellar mass of $2.98 \times 10^6 M_{\odot}$ of the UCD, which is $\sim 50\%$ lower than the $6.3 \times 10^6 M_{\odot}$ derived from the virial mass estimate based on the integrated dispersion from Taylor et al. (2010). Given that our integrated dispersion is consistent with theirs, this discrepancy appears to be due primarily to our mass modeling. Specifically, we find an effective radius of $r_{\text{eff}} = 5.17 \text{ pc}$, which is smaller than their $r_{\text{eff}} = 6.8 \text{ pc}$. Additional differences include their assumption of a virial factor compared to our more accurate MGE mass modeling. As noted above, with our best-fit $\Psi = 0.94$, our mass measurement places UCD 320 among the UCDs without elevated dynamical masses.

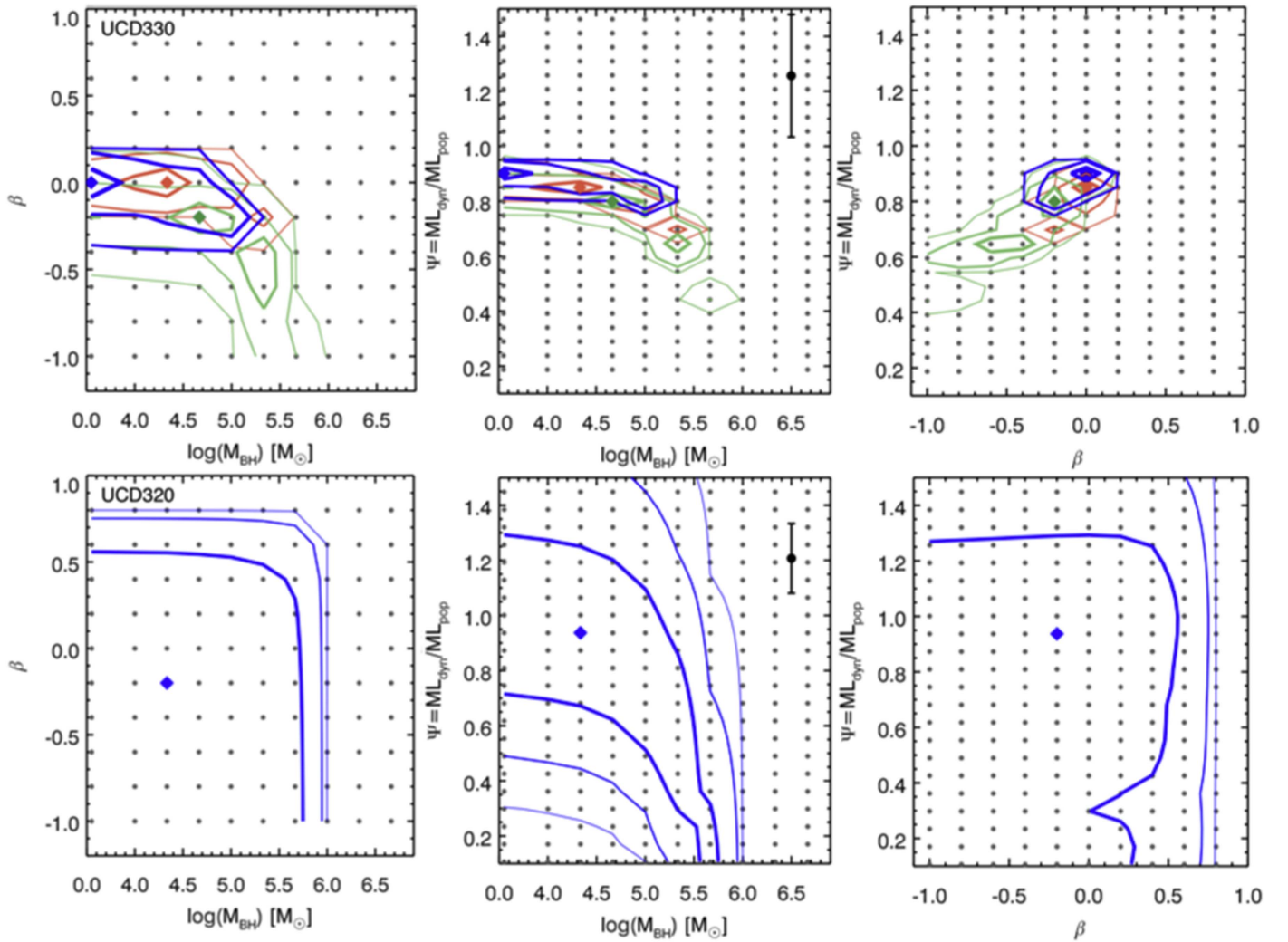


Figure 8. Two-dimensional likelihood contours show the dependence of anisotropy β , black hole mass M_* , and the normalized M/L ratio Ψ . The top row shows the panels for UCD 330 and the bottom row for UCD 320. In blue we show the likelihood contours for the 2D model, where the 1, 2, and 3 σ confidence levels have decreasing line thickness. For UCD 320, the blue contours show the results for model fits to the radial profile. The set of green contours shows the likelihood map for the radial dispersion profile for UCD 330, and the orange contours depict the situation when we just fit the upper half of the 2D dispersion map. The gray points mark each JAM model of the grid, and the blue and green diamonds are the best-fit model. The error bar in the middle panel of both UCDs indicates the systematic error in M_{pop} and thus Ψ due to the uncertainty of the metallicity.

We plot the results of the isotropic radial JAM models for UCD 320 in Figure 7 for several BH mass contributions. The best-fit BH mass model of 0.8% ($M_* = 2.15 \times 10^4 M_\odot$) is shown in green and the 3 σ upper limit on the BH mass of 37.7% ($1 \times 10^6 M_\odot$) is shown in red. Although we observe an increase in the dispersion in the very central bin, it is not significant because of its large error bar. The remaining dispersion profile is very flat at just above 20 km s^{-1} .

6. Discussion

In this work we have tested whether two lower mass UCDs in CenA host an SMBH in their centers (Taylor et al. 2010; Mieske et al. 2013), which would imply that they are the stripped nuclear star clusters of dwarf galaxies. From our dynamical modeling of adaptive optics kinematic data, we find that (1) no BHs are detected, and (2) no elevation in the mass-to-light ratios was found even for models with no BH, contrary to previous measurements (Taylor et al. 2010). In this section,

we discuss these results in the context of previous results and the implications for the formation of UCDs.

6.1. Upper Limits on BH Masses

We find that a BH larger than $M_* = 1.0 \times 10^5 M_\odot$ is excluded at a 3 σ confidence in UCD 330. This corresponds to 1.7% mass fraction. The dynamical models for UCD 320 place a 3 σ upper limit on a BH in UCD 320 at $M_* = 1.0 \times 10^6 M_\odot$, which corresponds to a BH mass fraction of 37.7%.

We have measurements of BH mass fractions of 13%, 15%, and 18% and in three massive UCDs (Seth et al. 2014; Ahn et al. 2017). The 1.7% 3 σ limit on the BH mass fraction in UCD 330 is significantly below these typical BH mass fractions. Thus it is clearly different from these massive UCDs with high mass fraction BHs. In UCD 320, our limit on the BH mass fraction is much higher, and the 37.7% indicates that a high mass fraction BH similar to those that have been previously discovered is still allowed by our models. All values for both UCDs are summarized in Table 4.

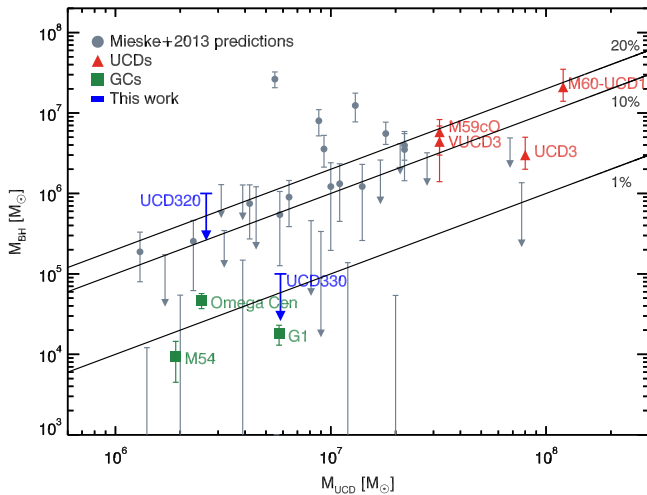


Figure 9. Comparison between UCD and GC masses and their central BHs. Gray points are the predictions and upper limits for UCDs based solely on their integrated dispersions from Mieske et al. (2013). Green squares are the measured BHs in GCs ω Cen, G1, and M54 taken from Lützgendorf et al. (2013). The four known BH masses in UCDs are plotted as red triangles and are taken from Seth et al. (2014), Ahn et al. (2017), and Afanasiev et al. (2018). The three black lines mark constant fractions of 1%, 10%, and 20% BH mass fraction, respectively.

There is evidence that UCD 320 hosts an X-ray source with an ultra-luminous peak flare luminosity of $9^{+4}_{-3} \times 10^{39} \text{ erg s}^{-1}$ (Irwin et al. 2016). While the sustained X-ray luminosity is consistent with a normal X-ray binary, the flaring luminosity could suggest a massive BH as it is brighter than the typical X-ray binary luminosities (She et al. 2017). Assuming that this flare is caused by an accreting BH, the X-ray flare timing places an upper limit of $2 \times 10^6 M_\odot$ on the BH mass. While the exact reason for the flare is unknown, their BH upper limit is consistent with ours, and thus a massive BH in UCD 320 is still possible.

In Figure 9 we compare existing BH mass measurements in GCs and UCDs to the upper limits in our two objects. We also added the predicted BH masses from Mieske et al. (2013) based on assuming that any M/L enhancement observed in a given UCD from integrated dispersion measurements is due to a BH. The black lines are a constant BH mass fraction of 1%, 10%, and 20%, respectively. Three of the massive UCDs (red) with measured BH masses are within the 10%–20% range. However, the possible intermediate-mass BHs detected in Local Group GCs show mass fractions of $<2\%$. Although these BH masses have been measured in several Local Group GCs (Ibata et al. 2009; Noyola et al. 2010; Lützgendorf et al. 2013; Baumgardt 2017), the BH signal is intrinsically degenerate, with significant radial anisotropy, and thus some of the detections remain controversial (van der Marel & Anderson 2010; Zocchi et al. 2017). The upper limit of UCD 320 is consistent with a such a 10%–20% BH mass fraction, and thus is not constraining, but in UCD 330, only a source similar to the Local Group GCs intermediate-mass BHs could be present. We note that when we include all the data from Mieske et al. (2013), there seems to be a trend of lower mass fraction BHs in lower mass UCDs; our upper limits are fully consistent with this trend.

6.2. Mass-to-light Ratios

In this work we have shown that contrary to previous findings, UCD 320 and UCD 330 have M/L ratios that are not inflated. In both cases, our best-fit models are completely

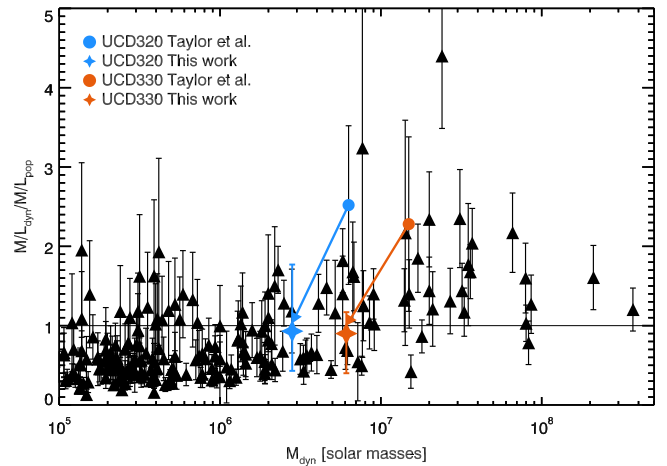


Figure 10. Ratio of M/L_{dyn} over the stellar population prediction M/L_{pop} plotted vs. the stellar mass of GCs and UCDs. The black data points are mainly from Mieske et al. (2013) with updated values for M60-UCD1 (Seth et al. 2014), M59cO and VUCD3 (Ahn et al. 2017), and M59-UCD3 (Liu et al. 2015). The colored circles denote the measured values from Taylor et al. (2010) for the two UCDs, and the stars mark the new measured Ψ values from this work, with an arrow marking the change toward the new measurements. The black line is where M/L_{dyn} is exactly equal to the expected stellar population M/L_{pop} .

consistent with their stellar populations within the errors, at $\Psi = \frac{M_{\text{dyn}}}{M_{\text{pop}}} = 0.9$ (blue and orange diamond symbols in Figure 10). In this context, the lack of detectable BHs in these systems is not surprising, as in a majority of the more massive UCDs with detected BHs, the best-fit models without a BH mass have $\Psi > 1$ (Mieske et al. 2013; Seth et al. 2014; Ahn et al. 2017). This suggests that finding an inflated M/L does appear to be a strong indicator of the presence of a BH.

At the same time, our results point to the challenges of accurately measuring the dynamical M/L s from integrated dispersions. In UCD 330, the higher velocity dispersion of 41.5 km s^{-1} found by Taylor et al. (2010) yielded an M/L_V of $6.3^{+1.6}_{-1.7}$, giving a $\Psi = 2.3$. Remodeling of this cluster using the Taylor et al. (2010) dispersion by Mieske et al. (2013) yielded a somewhat lower, but still significantly inflated $\Psi = 1.7$. Our much lower $\Psi = 0.9^{+0.3}_{-0.6}$ (and $M/L_V = 2.97^{+0.2}_{-0.5}$) value results primarily from our lower dispersion, but may also be due in part to our two-component mass model. As discussed above, our lower dispersion is consistent with the previously published dispersion of Rejkuba et al. (2007) based on analysis of the same data as presented in Taylor et al. (2010).

In UCD 320, we also find a much lower value than previous measurements, but for different reasons. Taylor measured an $M/L_V = 5.3^{+0.8}_{-1.0}$; because of the lower metallicity of this system relative to UCD 330, this resulted in an even higher estimate of $\Psi = 2.5$; while the Mieske et al. (2013) analysis found $\Psi = 1.6$. In this case, our lower Ψ value appears to come in part from our smaller derived effective radius of 5.2 pc, while Taylor et al. (2010) use a significantly higher 6.8 pc derived from estimates of Harris et al. (2002) from STIS data. We also note that our and the Mieske et al. (2013) lower Ψ values relative to Taylor et al. (2010) results are in part due to higher population M/L estimates; Taylor et al. (2010) uses the Bruzual & Charlot (2003) models, while Mieske et al. (2013) defines a somewhat higher M/L versus $[\text{Fe}/\text{H}]$ relation that we also use in this paper.

From our findings here, in combination with the much lower M/L found in M59cO by Ahn et al. (2017) relative to previous integrated-light studies, it is clear that at least some fraction of the integrated-light M/L s are not well determined. In general, there appears to be a bias toward overestimating the M/L . This could be due to overestimation of the dispersion, perhaps due to galaxy light contaminating the integrated-light spectra of the UCD, errors in the light/mass profile determination of the UCDs, or modeling errors. Modeling of adaptive optics data with *HST*-based mass models is therefore key to assessing the reliability of previous integrated measurements.

6.3. Are UCD 330 and 320 Stripped Nuclei?

In this work, we have presented the first adaptive optics measurements of UCDs below $10^7 M_\odot$. Adaptive optics measurements of massive UCDs ($>10^7 M_\odot$) have found high-mass fraction BHs in all systems studied thus far (Seth et al. 2014; Ahn et al. 2017; Afanasiev et al. 2018). These observations, combined with the higher-than-expected integrated dispersion mass-to-light ratios in most of these systems (Mieske et al. 2013), suggest that a large portion of these UCDs have massive BHs. This strongly supports the assumption that many of these UCDs are stripped nuclei. Simulations of tidal stripping in cluster environments have shown that the predicted number of massive UCDs $\gtrsim 2 \times 10^7 M_\odot$ is consistent with the observed numbers in Virgo and Fornax (Pfeffer et al. 2014, 2016). At lower masses, a larger fraction of UCDs are likely to be “ordinary” GCs, not stripped nuclei, but this fraction is likely dependent on environment.

Any lower mass stripped nuclei probably originate from lower mass galaxies because of the scaling relation between NSCs and BHs (e.g., Ferrarese et al. 2006; Scott & Graham 2013). Assuming a UCD mass equal to the NSC mass, the compilation of Georgiev et al. (2016) suggests that NSCs in the mass range of our objects ($2.5\text{--}6 \times 10^6 M_\odot$) have host galaxy stellar masses between $\sim 10^8$ and $5 \times 10^{10} M_\odot$. The occupation fraction of BHs in this mass range of galaxies is not yet well known. Above $\sim 10^9 M_\odot$, the BH occupation fraction appears quite high in early-type galaxies (Miller et al. 2015; Nguyen et al. 2017), but the Local Group galaxies M33 and NGC 205 host no BHs above $\sim 10^4 M_\odot$ (Gebhardt et al. 2001; Valluri et al. 2005), while BHs of about this mass have been claimed in the likely stripped nuclei M54 and ω Cen and G1 (Ibata et al. 2009; Noyola et al. 2010; Lützgendorf et al. 2013). Our upper limits in UCD 320 and UCD 330 do not exclude these intermediate-mass BHs, and thus our observations do not rule out that these objects could be the stripped nuclei of relatively low-mass galaxies $\lesssim 10^9 M_\odot$.

Another signature that may provide clues about whether these objects are stripped nuclei is their metallicity. With $[\text{Fe}/\text{H}] = -0.36$ and -0.85 for UCD 330 and UCD 320, both objects have a significantly lower metallicity than any of the four high-mass UCDs with BHs, which all have at least solar metallicity. The high metallicities for all UCDs above $\sim 3 \times 10^7 M_\odot$ were also suggested to be evidence for stripping in these systems by Janz et al. (2016). Assuming that our systems are stripped nuclei, we can try to constrain their host masses based on their metallicities.

The mass-metallicity relation of Lee et al. (2006) suggests galaxy masses of $\sim 10^9 M_\odot$ for UCD 330 and $2 \times 10^7 M_\odot$ for UCD 320. However, these are quite rough estimates, as the scatter in these relations is roughly an order of magnitude (Tremonti et al. 2004). Paudel et al. (2011) find nuclei with

metallicities consistent with UCD 320 in $\sim 10^9 M_\odot$ galaxies. For the case of UCD 330, its mass and metallicity are fully consistent with being a stripped nucleus, while for UCD 320, its NSC would have to have been on the metal-poor end of the distribution given the mass of the NSC. However, their metallicities are also consistent with these objects being ordinary GCs.

We reanalyzed UVES data for UCD 320 and UCD 330 from Rejkuba et al. (2007) using the NBURSTS stellar population fitting code as described in Chilingarian et al. (2007). We find that the α -abundance of UCD 330 is $[\alpha/\text{Fe}] = +0.16 \pm 0.03$ dex, while that of UCD 320 is not well determined. The nuclei of dwarf galaxies are not significantly α -enhanced (Chilingarian 2009; Paudel et al. 2011), and thus our measurement of a moderate enhancement in UCD 330 implies that it would be consistent with being the nucleus of a dwarf galaxy progenitor. The four UCDs with confirmed BHs all have higher enhancement in their α -abundance between $[\alpha/\text{Fe}] = 0.2\text{--}0.5$ dex (Francis et al. 2012), indicating that they might originate from more massive progenitors, which have higher α -abundance enhancements (Thomas et al. 2005).

Rotation may also be a signature of stripped galaxy nuclei. Strong rotation is seen in nearby nuclear star clusters (Seth et al. 2008b; Seth 2010; Feldmeier et al. 2014; Nguyen et al. 2017), with V/σ values ranging between ~ 0.3 and 1.3 , with both early and late-type galaxies showing strong rotation. This rotation can be created through cluster merging, but the strongest rotation is likely to be due to in situ star formation (e.g., Hartmann et al. 2011; Tsatsi et al. 2017). Larger scale (~ 100 pc) nuclear disks are also common (Launhardt et al. 2002; Balcells et al. 2007; Chilingarian 2009; Morelli et al. 2010; Toloba et al. 2014), and stripping of these could also yield rotating UCDs. On the other hand, GCs typically do not rotate this strongly, with typical $V/\sigma \lesssim 0.2$ (Lane et al. 2010; Bellazzini et al. 2012; Fabricius et al. 2014; Kimmig et al. 2015; Kamann et al. 2018). Given the measured V/σ of UCD 330 and UCD 320 of 0.3 and 0.4 , respectively, this relatively strong rotation may argue in favor of these objects being stripped nuclei. However, we caution that increasing rotation is also seen at longer relaxation times (Kamann et al. 2018), and our systems have longer relaxation times than most MW GCs (half-light radius t_{rel} of 2.8 Gyr for UCD 330 and 6.0 Gyr for UCD 320).

Finally, many UCDs, including UCD 330, have two-component profiles, extra-tidal light, or tidal tails (Martini & Ho 2004; Evstigneeva et al. 2007; Voggel et al. 2016; Wittmann et al. 2016). These are expected for stripped galaxy nuclei, as the inner component tracks the original NSC, while the outer section is the remnants of the remaining galaxy (Pfeffer & Baumgardt 2013). Low surface brightness halos found around galactic GCs have also been suggested to track tidally stripped nuclei (e.g., Olszewski et al. 2009; Kuzma et al. 2018). Thus the two-component profile provides perhaps the strongest evidence for UCD 330 being a stripped nucleus.

In summary, the lack of massive BHs in UCD 330 and UCD 320 does not imply that these systems are not stripped nuclei. The relatively strong rotation and the two-component structure in UCD 330 do support the idea that these UCDs may be stripped nuclei. If they are stripped nuclei, they would probably come from low-mass galaxies, for which the BH demographics are not yet well understood.

7. Conclusions

This study is the first to target lower mass UCDs ($<10^7 M_\odot$) in the search of central massive BHs, which would be strong evidence that they are the former nuclear star clusters of stripped dwarf galaxies. We constrained the BHs in these systems using dynamical modeling of stellar kinematic measurements from adaptive optics assisted VLT/SINFONI data. We detected no BHs, but we can place a 3σ upper limit on the BH masses. We find an upper limit of $M_* = 1.0 \times 10^5 M_\odot$ for UCD 330 and $M_* = 1.0 \times 10^6 M_\odot$ for UCD 320. This corresponds to relative mass fractions of 1.7% and 37.7%, respectively, with the poorer constraint in UCD 320 resulting from significantly lower data quality. The 1.7% mass fraction upper limit in UCD 330 excludes the presence of a high mass fraction (10%–20%) BH, similar to those found in more massive UCDs (Seth et al. 2014; Ahn et al. 2017; Afanasiev et al. 2018), but an intermediate-mass BH similar to those claimed in Local Group GCs (Ibata et al. 2009; Noyola et al. 2010; Lützgendorf et al. 2013) cannot be excluded.

We have shown that the dynamical M/L of UCD 320 and UCD 330 are not inflated, and for both UCDS, our models are fully consistent with predictions from stellar population models with $\Psi = \frac{M_{\text{dyn}}}{M_{\text{pop}}} = 0.9$ within the error bars. In most of the UCDs with measured massive BHs, the best-fit models without a BH suggest that they are overmassive, with $\Psi > 1$ (Mieske et al. 2013; Seth et al. 2014; Ahn et al. 2017). Therefore, our BH non-detections in these low-mass UCDs support the hypothesis that the inflated integrated-light dynamical M/L found in many UCDs does indicate the presence of a high mass fraction BH.







Our study finds that the two UCDs rotate significantly, which is often observed for nuclear star clusters, but rarely for GCs. Furthermore, the surface brightness profile of UCD 330 is best fit by a two-component model, as expected for stripped nuclei. In UCD 320, the high BH mass upper limit, combined with the X-ray source detected there, still leaves room for this system to host a significant BH. Therefore, there is some support that these two UCDs may in fact be stripped dwarf galaxy nuclei.

With our upcoming program on SINFONI, we will be able to test for the presence of a BH in three more low-mass UCDs, which will more than double the sample of low-mass UCDs with resolved kinematics. We will be able to detect any potential BHs in them down to $2.0 \times 10^5 M_\odot$. This will help to further establish whether stripped galaxy nuclei exist among low-mass UCDs and to determine how the SMBH occupation fraction varies with UCD mass.

Work on this project by K.T.V. and A.C.S. was supported by AST-1350389. J.S. acknowledges support from NSF grant AST-1514763 and the Packard Foundation. A.J.R. was supported by National Science Foundation grant AST-1515084 and as a Research Corporation for Science Advancement Cottrell Scholar. I.C.’s research is supported by the Telescope Data Center, Smithsonian Astrophysical Observatory. I.C. also acknowledges support by the Russian Science Foundation grant 17-72-20119 and by the ESO Visiting Scientist programme. Based on observations made with the NASA/ESA *Hubble Space Telescope*, and obtained from the Hubble Legacy Archive, which is a collaboration between the Space Telescope Science Institute (STScI/NASA), the Space Telescope European Coordinating Facility (ST-ECF/ESA) and the Canadian Astronomy Data Centre (CADC/NRC/CSA).

Facilities: HST, VLT/SINFONI.

ORCID iDs

Karina T. Voggel  <https://orcid.org/0000-0001-6215-0950>
 Nadine Neumayer  <https://orcid.org/0000-0002-6922-2598>
 Igor Chilingarian  <https://orcid.org/0000-0002-7924-3253>
 Christopher Ahn  <https://orcid.org/0000-0002-9852-2258>
 Dieu D. Nguyen  <https://orcid.org/0000-0002-5678-1008>
 Aaron J. Romanowsky  <https://orcid.org/0000-0003-2473-0369>
 Jonelle L. Walsh  <https://orcid.org/0000-0002-1881-5908>
 Jay Strader  <https://orcid.org/0000-0002-1468-9668>

References

- Afanasiev, A. V., Chilingarian, I. V., Mieske, S., et al. 2018, *MNRAS*, in press (doi:[10.1093/mnras/sty913](https://doi.org/10.1093/mnras/sty913))
- Ahn, C. P., Seth, A. C., den Brok, M., et al. 2017, *ApJ*, **839**, 72
- Balcells, M., Graham, A. W., & Peletier, R. F. 2007, *ApJ*, **665**, 1084
- Bastian, N., Saglia, R. P., Goudfrootij, P., et al. 2006, *A&A*, **448**, 881
- Baumgardt, H. 2017, *MNRAS*, **464**, 2174
- Beasley, M. A., Bridges, T., Peng, E., et al. 2008, *MNRAS*, **386**, 1443
- Bekki, K., Couch, W. J., Drinkwater, M. J., & Shioya, Y. 2003, *MNRAS*, **344**, 399
- Bellazzini, M., Dalessandro, E., Sollima, A., & Ibata, R. 2012, *MNRAS*, **423**, 844
- Binney, J. 1978, *MNRAS*, **183**, 501
- Brodie, J. P., Romanowsky, A. J., Strader, J., & Forbes, D. A. 2011, *AJ*, **142**, 199
- Bruzual, G., & Charlot, S. 2003, *MNRAS*, **344**, 1000
- Cappellari, M. 2002, *MNRAS*, **333**, 400
- Cappellari, M. 2008, *MNRAS*, **390**, 71
- Cappellari, M. 2017, *MNRAS*, **466**, 798
- Cappellari, M., & Copin, Y. 2003, *MNRAS*, **342**, 345
- Cappellari, M., & Emsellem, E. 2004, *PASP*, **116**, 138
- Carretta, E., Bragaglia, A., Gratton, R. G., et al. 2010, *ApJL*, **714**, L7
- Chilingarian, I. V. 2009, *MNRAS*, **394**, 1229
- Chilingarian, I. V., Prugniel, P., Sil’chenko, O. K., & Afanasiev, V. L. 2007, *MNRAS*, **376**, 1033
- Da Rocha, C., Mieske, S., Georgiev, I. Y., et al. 2011, *A&A*, **525**, A86
- Drinkwater, M. J., Gregg, M. D., Hilker, M., et al. 2003, *Natur*, **423**, 519
- Drinkwater, M. J., Jones, J. B., Gregg, M. D., & Phillips, S. 2000, *PASA*, **17**, 227
- Eisenhauer, F., Abuter, R., Bickert, K., et al. 2003, *Proc. SPIE*, **4841**, 1548
- Evstigneeva, E. A., Gregg, M. D., Drinkwater, M. J., & Hilker, M. 2007, *AJ*, **133**, 1722
- Fabricius, M. H., Noyola, E., Rukdee, S., et al. 2014, *ApJL*, **787**, L26
- Feldmeier, A., Neumayer, N., Seth, A., et al. 2014, *A&A*, **570**, A2
- Ferrarese, L., Côté, P., Jordán, A., et al. 2006, *ApJS*, **164**, 334
- Francis, K. J., Drinkwater, M. J., Chilingarian, I. V., Bolt, A. M., & Firth, P. 2012, *MNRAS*, **425**, 325
- Gebhardt, K., Lauer, T. R., Kormendy, J., et al. 2001, *AJ*, **122**, 2469
- Georgiev, I. Y., Böker, T., Leigh, N., Lützgendorf, N., & Neumayer, N. 2016, *MNRAS*, **457**, 2122
- Girardi, L., Bressan, A., Bertelli, G., & Chiosi, C. 2000, *A&AS*, **141**, 371
- Graham, A. W., & Spitler, L. R. 2009, *MNRAS*, **397**, 2148
- Harris, G. L. H., Geisler, D., Harris, H. C., & Hesser, J. E. 1992, *AJ*, **104**, 613
- Harris, G. L. H., Rejkuba, M., & Harris, W. E. 2010, *PASA*, **27**, 457
- Harris, W. E., Harris, G. L. H., Holland, S. T., & McLaughlin, D. E. 2002, *AJ*, **124**, 1435
- Hartmann, M., Debattista, V. P., Seth, A., Cappellari, M., & Quinn, T. R. 2011, *MNRAS*, **418**, 2697
- Hernandez, S., Larsen, S., Trager, S., Kaper, L., & Groot, P. 2018, *MNRAS*, **476**, 5189
- Hilker, M. 2006, arXiv:[astro-ph/0605447](https://arxiv.org/abs/astro-ph/0605447)
- Hilker, M., Infante, L., Vieira, G., Kissler-Patig, M., & Richtler, T. 1999, *A&AS*, **134**, 75
- Hilker, M., Kayser, A., Richtler, T., & Willemsen, P. 2004, *A&A*, **422**, L9
- Ibata, R., Bellazzini, M., Chapman, S. C., et al. 2009, *ApJL*, **699**, L169
- Irwin, J. A., Maksym, W. P., Sivakoff, G. R., et al. 2016, *Natur*, **538**, 356
- Janz, J., Norris, M. A., Forbes, D. A., et al. 2016, *MNRAS*, **456**, 617
- Jennings, Z. G., Romanowsky, A. J., Brodie, J. P., et al. 2015, *ApJL*, **812**, L10
- Kamann, S., Husser, T.-O., Dreizler, S., et al. 2018, *MNRAS*, **473**, 5591
- Kimmig, B., Seth, A., Ivans, I. I., et al. 2015, *AJ*, **149**, 53
- Kuzma, P. B., Da Costa, G. S., & Mackey, A. D. 2018, *MNRAS*, **473**, 2881

- Lane, R. R., Kiss, L. L., Lewis, G. F., et al. 2010, *MNRAS*, **406**, 2732
- Launhardt, R., Zylka, R., & Mezger, P. G. 2002, *A&A*, **384**, 112
- Lee, H., Skillman, E. D., Cannon, J. M., et al. 2006, *ApJ*, **647**, 970
- Liu, C., Peng, E. W., Toloba, E., et al. 2015, *ApJL*, **812**, L2
- Lützgendorf, N., Kissler-Patig, M., Neumayer, N., et al. 2013, *A&A*, **555**, A26
- Maraston, C. 2005, *MNRAS*, **362**, 799
- Maraston, C., Bastian, N., Saglia, R. P., et al. 2004, *A&A*, **416**, 467
- Martini, P., & Ho, L. C. 2004, *ApJ*, **610**, 233
- Mieske, S., Frank, M. J., Baumgardt, H., et al. 2013, *A&A*, **558**, A14
- Mieske, S., Hilker, M., & Infante, L. 2004, *A&A*, **418**, 445
- Mieske, S., Hilker, M., & Misgeld, I. 2012, *A&A*, **537**, A3
- Miller, B. P., Gallo, E., Greene, J. E., et al. 2015, *ApJ*, **799**, 98
- Minniti, D., Kissler-Patig, M., Goudfrooij, P., & Meylan, G. 1998, *AJ*, **115**, 121
- Misgeld, I., & Hilker, M. 2011, *MNRAS*, **414**, 3699
- Morelli, L., Cesetti, M., Corsini, E. M., et al. 2010, *A&A*, **518**, A32
- Murray, N. 2009, *ApJ*, **691**, 946
- Nguyen, D. D., Seth, A. C., Neumayer, N., et al. 2017, eprint (arXiv:1711.04314)
- Norris, M. A., Escudero, C. G., Faifer, F. R., et al. 2015, *MNRAS*, **451**, 3615
- Norris, M. A., & Kannappan, S. J. 2011, *MNRAS*, **414**, 739
- Norris, M. A., Kannappan, S. J., Forbes, D. A., et al. 2014, *MNRAS*, **443**, 1151
- Noyola, E., Gebhardt, K., Kissler-Patig, M., et al. 2010, *ApJL*, **719**, L60
- Olszewski, E. W., Saha, A., Knezek, P., et al. 2009, *AJ*, **138**, 1570
- Paudel, S., Lisker, T., & Kuntschner, H. 2011, *MNRAS*, **413**, 1764
- Peng, C. Y., Ho, L. C., Impey, C. D., & Rix, H.-W. 2002, *AJ*, **124**, 266
- Pfeffer, J., & Baumgardt, H. 2013, *MNRAS*, **433**, 1997
- Pfeffer, J., Griffen, B. F., Baumgardt, H., & Hilker, M. 2014, *MNRAS*, **444**, 3670
- Pfeffer, J., Hilker, M., Baumgardt, H., & Griffen, B. F. 2016, *MNRAS*, **458**, 2492
- Rejkuba, M., Dubath, P., Minniti, D., & Meylan, G. 2007, *A&A*, **469**, 147
- Renaud, F., Bournaud, F., & Duc, P.-A. 2015, *MNRAS*, **446**, 2038
- Rossa, J., van der Marel, R. P., Böker, T., et al. 2006, *AJ*, **132**, 1074
- Schulz, C., Pflamm-Altenburg, J., & Kroupa, P. 2015, *A&A*, **582**, A93
- Schweizer, F., Seitzer, P., Whitmore, B. C., Kelson, D. D., & Villanueva, E. V. 2018, *ApJ*, **853**, 54
- Scott, N., & Graham, A. W. 2013, *ApJ*, **763**, 76
- Seth, A., Agüeros, M., Lee, D., & Basu-Zych, A. 2008a, *ApJ*, **678**, 116
- Seth, A. C. 2010, *ApJ*, **725**, 670
- Seth, A. C., Blum, R. D., Bastian, N., Caldwell, N., & Debattista, V. P. 2008b, *ApJ*, **687**, 997
- Seth, A. C., Dalcanton, J. J., Hodge, P. W., & Debattista, V. P. 2006, *AJ*, **132**, 2539
- Seth, A. C., van den Bosch, R., Mieske, S., et al. 2014, *Natur*, **513**, 398
- She, R., Ho, L. C., & Feng, H. 2017, *ApJ*, **842**, 131
- Siegel, M. H., Dotter, A., Majewski, S. R., et al. 2007, *ApJL*, **667**, L57
- Taylor, M. A., Puzia, T. H., Harris, G. L., et al. 2010, *ApJ*, **712**, 1191
- Thomas, D., Maraston, C., Bender, R., & Mendes de Oliveira, C. 2005, *ApJ*, **621**, 673
- Toloba, E., Guhathakurta, P., van de Ven, G., et al. 2014, *ApJ*, **783**, 120
- Tremonti, C. A., Heckman, T. M., Kauffmann, G., et al. 2004, *ApJ*, **613**, 898
- Tsatsi, A., Mastrobuono-Battisti, A., van de Ven, G., et al. 2017, *MNRAS*, **464**, 3720
- Valluri, M., Ferrarese, L., Merritt, D., & Joseph, C. L. 2005, *ApJ*, **628**, 137
- van der Marel, R. P., & Anderson, J. 2010, *ApJ*, **710**, 1063
- Voggel, K., Hilker, M., & Richtler, T. 2016, *A&A*, **586**, A102
- Walcher, C. J., Böker, T., Charlot, S., et al. 2006, *ApJ*, **649**, 692
- Wallace, L., & Hinkle, K. 1996, *ApJS*, **107**, 312
- Wittmann, C., Lisker, T., Pasquali, A., Hilker, M., & Grebel, E. K. 2016, *MNRAS*, **459**, 4450
- Zocchi, A., Gieles, M., & Hénault-Brunet, V. 2017, *MNRAS*, **468**, 4429